

Curvatures and inhomogeneities: An improved common-reflection-surface approach

Benjamin Schwarz*, Claudia Vanelle*, Dirk Gajewski*, and Boris Kashtan[†]

** Institute of Geophysics, University of Hamburg,
Bundesstr. 55, 20146 Hamburg, Germany*

*[†] Faculty of Physics, St. Petersburg State University,
1 Ulyanovskaya St., St. Petersburg 198504, Russian Federation*

(March 19, 2019)

Running head: **Implicit common reflection surface**

ABSTRACT

Multi-parameter stacking is an important tool to obtain a first reliable time image of the subsurface. In addition, it provides wavefield attributes, which form the basis for many important applications. The quality of the image and the attribute estimates heavily relies on the accuracy of the traveltime moveout description. The commonly-used hyperbolic common reflection surface (CRS) operator reduces to the NMO hyperbola in the CMP gather. Its accuracy, however, depends on the curvature of the reflector under consideration. The conventional multifocusing operator, a time-shifted double-square-root expression, leads to good results for high reflector curvatures and moderate inhomogeneities of the overburden. We present a new implicit CRS formulation that combines the robustness of CRS regarding heterogeneities with the high sensitivity to curvature of the multifocusing approach. It assumes reflectors to be locally circular and can be applied in an iterative fashion. For simple but common acquisition and subsurface configurations, the new traveltime expression

reduces to familiar formulae. Quantitative studies reveal that the new operator performs equally well over the full range of curvatures even in the presence of strong heterogeneities, while providing higher accuracy than the conventional CRS and multifocusing methods. In addition, its application results in more reliable attribute estimates and an improved time-migrated section. Comparison of stacking and migration results for the complex synthetic Sigsbee 2a dataset confirms the potential of the suggested approach.

INTRODUCTION

Stacking plays a crucial role in seismic data processing. The procedure itself allows to considerably decrease the redundancy of the data, resulting in an improved signal-to-noise ratio and a first interpretable time image. In addition, it provides attributes of the wavefield, which form the basis of many subsequent processing steps. In the still most-widely used classical approach (Mayne, 1962), coherent energy is summed within just one single CMP gather. Since neighboring CMPs carry information about the same subsurface region, the concept of the common reflection surface (CRS) stack was developed by Jäger et al. (2001) as a reasonable extension to fully exploit the information contained in the prestack data.

In current implementations of the CRS stack, traveltime moveout is described by a hyperbolic expression (Schleicher et al., 1993; Jäger et al., 2001) formulated in terms of three kinematic attributes (Hubral, 1983). These allow for many powerful applications, ranging from multiple suppression (Dümmong and Gajewski, 2008) over prestack data enhancement and regularization (Baykulov et al., 2011) to velocity model building for depth migration (Duvencak, 2004). The quality of the stacking results heavily relies on the accuracy of the traveltime moveout description. Hyperbolic moveout as a function of offset is only exact for the case of a planar dipping reflector beneath a homogeneous overburden. Any deviation from this simple assumption results in the moveout becoming nonhyperbolic (Fomel and Grechka, 2001).

It can thus be shown that the hyperbolic CRS expression is not ideally suited for imaging diffractions or reflectors of high curvature. Since, however, the imaging of small objects plays an important role in complex geological settings, the classical multifocusing (MF) formula (Gelchinsky et al., 1999), a double-square-root-based approximation, has gained increased

attention in recent years. Although it is parameterized with the same attributes as the CRS operator, we find that the accuracy of the multifocusing moveout appears to be more affected by strong velocity gradients, i.e., heterogeneities in the overburden.

In this work, we present a new implicit CRS (i-CRS) approach that combines the stable performance of the CRS method for stronger velocity gradients and the high accuracy of multifocusing for diffractions. The most intuitive way to extend the hyperbolic formulae, which are suited for plane reflectors, is to assume a locally circular reflector in a constant velocity medium. While Fomel and Kazinnik (2012) presented a closed-form solution for a hyperbolic reflector model, Höcht et al. (1999) and Landa et al. (2010) considered a circular or spherical reflecting interface.

The finite constant curvature is geometrically appealing and naturally spans the practically important cases of a planar reflector and a point diffractor. While Höcht et al. (1999) presented parametric expressions, Landa et al. (2010), following Drexler and Gander (1998), provided the analytical solution to the circular reflector problem. Both lead to exact traveltimes for the constant velocity case. Since these approaches are either computationally demanding or require trace interpolation, they are not well suited for efficient implementation. In both, conventional multifocusing and the extended approach by Landa et al. (2010), heterogeneity is handled by the application of a time-shift, revealing the strong link of these methods to the shifted hyperbola by de Bazelaire (1988).

Based on the work of Vanelle et al. (2012) and Schwarz et al. (2012), we introduce an implicit solution to the circular reflector problem that is easy to implement and can be applied efficiently in an iterative fashion. Whereas the new approach is based on the same assumptions as the extended multifocusing approach by Landa et al. (2010) and the

parametric expressions of Höcht et al. (1999), we establish a conceptually different CRS-like incorporation of the kinematic attributes by means of a coefficient matching procedure based on a Taylor series expansion. Thus, we combine the sensitivity to curvature of the multifocusing method with the robustness of CRS with respect to heterogeneity.

We investigate the new operator’s accuracy in terms of traveltime fit, parameter determination, and semblance in a quantitative study, and compare it to the original CRS and the multifocusing operator by Gelchinsky et al. (1999). For simple generic examples, the new operators performance is compared to the exact reference. In addition, we apply the three operators to the complex Sigsbee 2a synthetic data set. We demonstrate that the implicit CRS operator leads to a better stack result in terms of coherence and resolution. Furthermore, we carry out an approximate poststack time migration (Mann, 2002) using the mapping equations and the wavefield attributes of the considered methods. Again, the new approach leads to better results than the other techniques.

CONVENTIONAL CRS AND MULTIFOCUSING

As we have outlined in the introduction, the CRS as well as the multifocusing operators are based on the same set of attributes of the recorded wavefield. The three parameters α , R_{NIP} , and R_N were introduced by Hubral (1983) and can be interpreted appealingly in the framework of geometrical optics (Höcht et al., 1999). The quantities R_{NIP} and R_N are the radii of curvature of two so-called eigenwaves (Tygel et al., 1997). The NIP-wave (see Figure 1) stems from a fictitious point source placed at the point of normal incidence (NIP) on the reflector, and the normal or N-wave is the result of a fictitious exploding reflector experiment in the vicinity of NIP. Both waves emerge with the angle α at the horizontal zero-offset position x_0 and contain distinct properties of the reflector, i.e. its distance, curvature,

and orientation, propagated to the registration surface. Since these properties are measured at the surface, they are directly linked to traveltimes derivatives (e.g., Hertweck et al., 2007). Thus, CRS and multifocusing can be considered macro-velocity model independent, purely data-driven alternatives of the NMO/DMO process (e.g., Mann, 2002). For both methods, traces from neighboring CMPs are considered in the summation process, which results in an improved signal-to-noise ratio.

[Figure 1 about here.]

Conventional CRS

Traveltimes are commonly expressed by hyperbolic formulae (e.g., Jäger et al., 2001). Resulting from paraxial ray theory, these are second-order Taylor series expansions of the squared traveltimes. In midpoint ($\Delta x_m = x_m - x_0$) and half-offset (h) coordinates, using the parameters introduced above, the CRS operator reads,

$$t^2(\Delta x_m, h) = \left(t_0 + \frac{2 \sin \alpha}{v_0} \Delta x_m \right)^2 + \frac{2 t_0 \cos^2 \alpha}{v_0} \left(\frac{\Delta x_m^2}{R_N} + \frac{h^2}{R_{NIP}} \right) , \quad (1)$$

where t_0 is the zero-offset traveltimes, x_0 is the central midpoint location and v_0 denotes the overburden velocity near the surface. In analogy to the classical CMP method (Mayne, 1962), the CRS traveltimes moveout $t - t_0$ is a function of the reference time t_0 .

Multifocusing

Gelchinsky et al. (1999) introduced a double-square-root expression for the traveltimes that uses the same set of parameters as the CRS method. Their operator describes the traveltimes

of a reflection event in terms of the traveltime of a central ray and corrections applied at the source and receiver for a paraxial ray. It reads,

$$t(\Delta x_s, \Delta x_g) = t_0 + \Delta t_s + \Delta t_g \quad , \quad \text{with} \quad (2a)$$

$$\Delta t_s = \frac{\sqrt{R_s^2 + 2 R_s \Delta x_s \sin \alpha + \Delta x_s^2} - R_s}{v_0} \quad , \quad (2b)$$

$$\Delta t_g = \frac{\sqrt{R_g^2 + 2 R_g \Delta x_g \sin \alpha + \Delta x_g^2} - R_g}{v_0} \quad . \quad (2c)$$

The quantities R_s and R_g , with

$$R_s = \frac{1 + \sigma}{\frac{1}{R_N} + \frac{\sigma}{R_{NIP}}} \quad \text{and} \quad (3a)$$

$$R_g = \frac{1 - \sigma}{\frac{1}{R_N} - \frac{\sigma}{R_{NIP}}} \quad , \quad (3b)$$

are the radii of two hypothetical waves that focus at the intersection of the central and paraxial ray. Finally,

$$\sigma = \frac{\Delta x_s - \Delta x_g}{\Delta x_s + \Delta x_g + 2 \frac{\Delta x_s \Delta x_g}{R_{NIP}} \sin \alpha} \quad (4)$$

is the so-called focusing parameter. The distances $\Delta x_s = \Delta x_m - h$ and $\Delta x_g = \Delta x_m + h$ are the horizontal distances between the source and receiver, respectively, and the central midpoint location x_0 .

Landa et al. (2010) introduced an extension of the multifocusing moveout, which is based on the assumption of a locally spherical interface. In the frame of that work, they investigated the response from curved reflectors and concluded that the spherical approximation leads to higher traveltime and attribute accuracy. However, the work of Landa et al. (2010) also revealed that these improvements lose significance when heterogeneity is present in the overburden. Both, the conventional multifocusing approach and Landa's extension to spherical interfaces have in common that moveout is independent of the zero-offset reference

traveltime t_0 (e.g., Landa, 2007; Landa et al., 2010). This results in a time-shift notation of the total traveltime, which is conceptually different from the CRS approach. Since, in conclusion, the multifocusing formulae are closely related and the classical operator performs comparably for high curvatures (Landa et al., 2010), all comparisons in this work are based on formulae 2.

IMPLICIT COMMON REFLECTION SURFACE

Following the lines of Höcht et al. (1999) and Landa et al. (2010), we introduce the new traveltime surface based on the assumption of a circular reflecting interface in a constant velocity medium. The problem of finding the reflection point of a light ray on a circular mirror has a long history. According to written accounts, it can at least be traced back to the time of Ptolemy (Neumann, 1998). Various authors have since then stated that the coordinates of the reflection point for given start and end points can be gained by evaluating the roots of a fourth-order polynomial (e.g., Drexler and Gander, 1998).

[Figure 2 about here.]

We present a new implicit approach to find the reflection point by simple geometrical considerations and the application of Fermat’s principle of least time, following Vanelle et al. (2012). Figure 2 shows the geometrical setting of the problem. It suggests that the reflection point can be parameterized by the position (x_c, H) of the center of the circle, its radius R , and a polar angle denoted θ . All potential reflection points (x_r, z_r) are given by the equation of the circle,

$$(x_r - x_c)^2 + (H - z_r)^2 = R^2 \quad . \quad (5)$$

The total traveltime t in a medium with the constant velocity V is separated into two contributions, one stemming from the downgoing ray segment, t_s , the other from the upgoing ray segment, t_g . With

$$x_r = x_c + R \sin \theta \quad , \quad (6a)$$

$$z_r = H - R \cos \theta \quad , \quad (6b)$$

and by utilizing the Pythagorean theorem, we arrive at a double-square-root equation for the traveltime

$$t(\Delta x_m, h) = t_s + t_g \quad , \quad (7a)$$

$$t_s = \frac{\sqrt{(\Delta x_m - h - \Delta x_c - R \sin \theta)^2 + (H - R \cos \theta)^2}}{V} \quad , \quad (7b)$$

$$t_g = \frac{\sqrt{(\Delta x_m + h - \Delta x_c - R \sin \theta)^2 + (H - R \cos \theta)^2}}{V} \quad , \quad (7c)$$

where $\Delta x_c = x_c - x_0$. Please note that $\Delta x_m - \Delta x_c = x_m - x_c$.

Fermat's principle requires that the total reflection traveltime becomes minimal if θ describes an actual reflection point, and therefore

$$\frac{\partial t}{\partial \theta} = 0 \quad . \quad (8)$$

Assuming the overburden to be homogeneous and isotropic, solving for $\tan \theta$ leads to

$$\tan \theta = \frac{\Delta x_m - \Delta x_c}{H} + \frac{h}{H} \frac{t_s - t_g}{t_s + t_g} \quad . \quad (9)$$

Please note that although this expression is exact, it is also implicit since θ itself depends on the traveltime contributions t_s and t_g and vice versa.

In the zero-offset configuration, i.e., $h = 0$, the tangent of the angle θ_0 (see Figure 2(b)) can be derived from geometry only. It is, therefore, an entirely explicit expression,

$$\tan \theta_0 = \frac{\Delta x_m - \Delta x_c}{H} \quad . \quad (10)$$

Since it only depends on the coordinates of the middle point of the circle, θ_0 is a robust quantity and allows for an iterative application (Vanelle et al., 2012; Schwarz et al., 2012).

Accordingly, for the n -th iteration ($n = 1, 2, \dots$), equation 9 becomes

$$\tan \theta_n = \tan \theta_0 + \frac{h}{H} \frac{t_s(\theta_{n-1}) - t_g(\theta_{n-1})}{t_s(\theta_{n-1}) + t_g(\theta_{n-1})} \quad . \quad (11)$$

Figure 2(c) illustrates the iterative application. For the limiting case of $n \rightarrow \infty$ the iterated angle approaches its theoretical counterpart,

$$\lim_{n \rightarrow \infty} \theta_n = \theta \quad . \quad (12)$$

Heterogeneous media

While the initial parameterization is depth-related and only reflects the actual geometry for a homogeneous overburden, the operator can be extended to heterogeneous media. As we will demonstrate below, conventional CRS, in contrast to the classical multifocusing approach, is very robust with respect to heterogeneities in the overburden. While the curvature response is dominated by the overall mathematical shape of the operator (i.e., single- or double-square-root), the response to heterogeneity is steered by the incorporation of the parameters.

To merge the double-square-root shape of multifocusing with the incorporation of parameters in conventional CRS, we make use of the fact that equation 1 is a second-order approximation of the squared traveltimes. Squaring and expanding the traveltimes 7a and considering 7b and 7c leaves a set of four coefficients that are expressed in terms of V , x_c , H , and R . Comparing these coefficients to their respective counterparts in the CRS operator 1 results in a set of four equations with the following unique solution (Schwarz et al., 2012),

$$V = \frac{v_{NMO}}{\sqrt{1 + \frac{v_{NMO}^2}{v_0^2} \sin^2 \alpha}} \quad , \quad (13a)$$

$$x_c = x_0 - \frac{R_N \sin \alpha}{\cos^2 \alpha \left(1 + \frac{v_{NMO}^2}{v_0^2} \sin^2 \alpha\right)} \quad , \quad (13b)$$

$$H = \frac{v_0 R_N}{v_{NMO} \cos^2 \alpha \left(1 + \frac{v_{NMO}^2}{v_0^2} \sin^2 \alpha\right)} \quad , \quad (13c)$$

$$R = \frac{\frac{v_0 R_N}{v_{NMO} \cos^2 \alpha} - \frac{v_{NMO} t_0}{2}}{\sqrt{1 + \frac{v_{NMO}^2}{v_0^2} \sin^2 \alpha}} \quad , \quad (13d)$$

with the normal moveout velocity

$$v_{NMO} = \sqrt{\frac{2 v_0 R_{NIP}}{t_0 \cos^2 \alpha}} \quad . \quad (14)$$

Equations 13 establish a link to the surface-based CRS attributes. Our approach is thus a macro-velocity model independent imaging method valid for inhomogeneous media. Following from substitutions 13, we can observe that our parameterization, in contrast to the multifocusing formulae, is closely linked to the NMO concept, in which heterogeneity is handled by an effective velocity v_{NMO} . In accordance, the implicit CRS moveout, like for conventional CRS, is a function of the zero-offset traveltimes.

SPECIAL CASES

To obtain deeper insight into the character of the suggested implicit CRS operator, we investigate significant acquisition and subsurface configurations and compare the resulting i-CRS expressions with the according simplifications of conventional CRS and the multi-focusing operator 2. We begin with the diffraction case, which is crucial for application to time migration. This process relies on an accurate description of diffraction events in the prestack data. Furthermore, diffractions play an increasingly important role in seismic processing and interpretation (see, e.g., Khaidukov et al., 2004; Dell and Gajewski, 2011). Diffractions correspond to the limiting case of high reflector curvature. Since a stacking operator should be able to handle both, infinite and low reflector curvature, we also discuss the case of planar horizontal layering. To enable comparison with existing approaches, we confine ourselves to the description in the CMP gather for this setting.

Diffractions

A diffractor is, per definition, an object of infinite curvature relative to the predominant seismic wavelength. In consequence, the number of wavefield attributes needed to properly approximate the corresponding traveltime response reduces to two since $R_N = R_{NIP}$. As a result, the reflector radius R according to equation 13d is zero, and the diffraction traveltime t becomes entirely explicit. For normal incidence, i.e. $\alpha = 0$, the i-CRS formula reduces to the Kirchhoff time migration operator,

$$t = \sqrt{\frac{t_0^2}{4} + \frac{(\Delta x_m - h)^2}{v_{NMO}^2}} + \sqrt{\frac{t_0^2}{4} + \frac{(\Delta x_m + h)^2}{v_{NMO}^2}} \quad . \quad (15)$$

For the same setting, the conventional multifocusing traveltime is given by a shifted double-square-root expression,

$$t - t_0 + t_p = \sqrt{\frac{t_p^2}{4} + \frac{(\Delta x_m - h)^2}{v_0^2}} + \sqrt{\frac{t_p^2}{4} + \frac{(\Delta x_m + h)^2}{v_0^2}} \quad , \quad (16)$$

with $t_p = 2R_{NIP}/v_0$. In contrast to multifocusing and i-CRS, the conventional CRS operator maintains its hyperbolic shape, which is considered to be a less suitable description for prestack time migration.

In the zero-offset section, even for non-normal incidence, CRS and i-CRS approximate the diffraction response by the same hyperbolic expression (Mann, 2002; Schwarz et al., 2012),

$$t^2 = \frac{4H^2}{V^2} + \frac{4(x_m - x_c)^2}{V^2}, \quad (17)$$

with x_c , H and V according to equations 13, whereas the classical multifocusing formula becomes a time-shifted hyperbola (e.g., Keydar et al., 1990).

For the special case of a homogeneous medium, both i-CRS and multifocusing reduce to the same expressions and provide an exact description of the diffraction traveltimes. This means that the two methods vary only in the incorporation of the CRS attributes. Because of its hyperbolic shape, CRS differs from the other two approximations for the finite-offset case.

CMP gather, horizontal layering

When we assume horizontal layering in the subsurface (i.e, $\alpha = 0$ and $R_N = \infty$), i-CRS as well as the conventional CRS operator reduce to the classical hyperbolic expression in the

CMP gather (i.e., $\Delta x_m = 0$),

$$t^2 = t_0^2 + \frac{4h^2}{v_{RMS}^2} \quad , \quad (18)$$

where v_{RMS} is the root-mean-square (RMS) velocity.

In the i-CRS and the CRS formula, the RMS velocity is a combined parameter comprising R_{NIP} and t_0 , i.e., v_{RMS} is an effective property to account for the vertical velocity variations. In contrast, conventional multifocusing becomes the shifted hyperbola of de Bazelaire (1988), in which inhomogeneity is accounted for by the application of a shift in time (e.g., Landa, 2007).

QUANTITATIVE STUDIES

The simple model of a circular reflector below a constant vertical velocity gradient overburden allows for the forward calculation of the kinematic attributes. With these, the quality of each operator's estimate of α , R_{NIP} , and R_N gained in the stacking procedure can be evaluated. By prescribing the radius of the circle, R , we were able to investigate the impact of the reflector curvature on the accuracy of each operator.

[Figure 3 about here.]

This investigation was carried out for four different reflector radii ranging from $R = 10$ m, representing the limiting diffraction case, to $R = 10,000$ m, i.e., a nearly planar interface. The vertical depth of the top of the reflector, i.e., $H - R$, was kept constant at 1,000 m (see Figure 3). Since we consider constant vertical velocity gradient media, analytical ray tracing is applicable and was utilized for the generation of the datasets. We investigated

media with $v(z) = 2,000 \text{ m/s} + \gamma z$ and values for γ ranging from the constant velocity case, i.e., $\gamma=0/\text{s}$, to $\gamma=1.5/\text{s}$, representing strong vertical heterogeneity.

For all investigations, we have chosen a maximum offset of 2,000 m, i.e. a maximum offset-over-depth-ratio of two. The horizontal midpoint displacements from the center of the circle, $x_m - x_c$, range from -2,000 m to 2,000 m. Gaussian noise with a signal-to-noise ratio of 5 was added to the data. The datasets consist of 401 CMP gathers containing 81 traces each.

The parameters were determined by a semblance analysis. Difficulties arise if events cross, leading to the so-called conflicting dip problem. Based on the extended CRS implementation by Mann (2002), initial starting values for the simultaneous optimization were estimated by means of the so-called pragmatic approach. Although the detection of conflicting dips is, in principle, possible with this implementation, we could not achieve robust detection. Since this is a problem all considered techniques have in common, we decided to only image the strongest event at each zero-offset sample. While all offsets were considered for the stacking procedure, the midpoint aperture was kept constant at 500 m. In the following, we summarize our results for the performance of the individual operators regarding semblance, traveltimes, and parameter estimation. Finally, we have performed an attribute-based approximate poststack Kirchhoff time migration (as suggested by Mann, 2002) on the $R=10 \text{ m}$ data set in order to investigate how well the diffraction event can be collapsed by the parameters obtained from the different operators. Although this mapping technique provides rather noisy images in complex areas, it performs well when lateral heterogeneity is moderate. In the following, we use it as a tool to estimate the impact of the used traveltime operator on the quality of stack and attributes. While the diffraction response is utilized for CRS and i-CRS, the multifocusing-based migration uses the respective equation

by Keydar et al. (1990).

Number of iterations

[Figure 4 about here.]

Application of the new traveltime operator includes solving for the reflection point angle θ by utilizing an iterative scheme according to 11. Although this implicit approach potentially leads to less computational demands compared to the analytical solution, we want to ensure how many iterations prove to be sufficient for this generic, but more practical example. Figure 4 shows the RMS errors of i-CRS for low reflector curvature of $R = 10,000$ m as a function of the number of iterations and the gradient strength γ . While for the constant velocity case, the iterative scheme leads to very high accuracy up to machine precision, the refinement does not show any effect on the accuracy when vertical heterogeneity is present. This shows that in principle the exact solution by Landa et al. (2010) can be reached for the homogeneous case, but that traveltime errors due to the constant velocity assumption dominate for heterogeneous overburdens. Since even for non-vanishing gradients, the RMS errors of i-CRS are in the range of 0.1 %, we conclude that for practical application one iteration already provides sufficient accuracy. Thus, in all following examples the i-CRS reflection angle was only updated once.

Semblance

Since semblance can be considered a normalized measure of the quality of stack, we discuss the respective semblance sections. The stacked sections themselves display only very minor – if any – visible differences. Figure 5 shows the semblance value as a function of $x_m - x_c$

and gradient strength for the limiting cases of $R=10$ m, corresponding to a point diffractor, and $R=10,000$ m, describing an almost planar interface.

[Figure 5 about here.]

For the $R=10,000$ m case, all three operators perform well. For the diffraction limit, CRS provides a poorer fit for increasing $x_m - x_c$ than the two double-square-root-based stacking operators. This was expected because of the hyperbolic behavior of CRS in the offset direction. The semblance achieved with CRS, does, on the other hand not vary systematically with the strength of the gradient. Conventional multifocusing performs well even for large midpoint displacements from the diffraction’s apex. However, the semblance decreases for larger gradients. The i-CRS operator shows high semblance for strong gradients as well as large values of $x_m - x_c$.

Traveltimes

Figure 6 shows the RMS traveltimes errors of all three operators, displayed as a function of midpoint displacement and gradient strength. As expected, we observe in Figure 6(a) that the hyperbolic CRS expression accounts poorly for high reflector curvatures. This behavior confirms the insight gained by our considerations of the acquisition and subsurface configurations in the previous section. Due to its double-square-root shape, classical multifocusing provides a better fit than CRS for high curvatures, for values of R up to 1,000 m, and for all tested gradients. Only for $R = 10,000$ m, CRS performs comparable to multifocusing.

[Figure 6 about here.]

The comparison of i-CRS and conventional multifocusing in Figure 6(b), in turn, reveals

that the i-CRS approach handles inhomogeneity better than the shift-based parameterization of the multifocusing operator. In conclusion, the implicit CRS approach leads to higher accuracy than the other operators over the whole range of R and γ . This observation confirms that i-CRS combines indeed the benefits of conventional CRS and multifocusing, resulting in high accuracy for high as well as low reflector curvatures, and performing equally well for high and low velocity gradients.

Attributes

In Figure 7, the CRS parameters obtained with the three operators are displayed for $R=10$ m and $\gamma=0.5/\text{s}$. Comparison with the exact forward-calculated reference shows that all operators permit a good recovery of the angle α . The quality of the remaining parameters varies. Due to convergence issues in the optimization procedure, outliers exist in the displayed R_{NIP} , and $K_N = 1/R_N$ graphs, which is why we focus on the main trends of the parameters provided by the individual operators.

[Figure 7 about here.]

For small to moderate values of Δx_c , CRS systematically underestimates the radius R_{NIP} . For larger values, R_{NIP} fluctuates so strongly, that the main trend is hard to estimate, however, most values are significantly smaller than the reference. For K_N , we find a similar behavior. For small Δx_c , CRS leads to too small values of K_N , and for large Δx_c , K_N displays significant fluctuation, with an overall tendency to underestimate the exact value.

Conventional multifocusing leads to smoother graphs for R_{NIP} , and K_N with reasonable

accuracy for R_{NIP} and underestimation of K_N for small Δx_c . Towards higher, but even for moderate Δx_c , R_{NIP} is significantly underestimated and K_N is significantly overestimated.

The i-CRS operator yields the smoothest parameter curves. Although outliers exist, in particular for the parameter R_{NIP} , the results of i-CRS coincide with the exact results. The i-CRS operator is thus the only of the three that allows the reconstruction of the CRS parameters without systematic errors.

Although not displayed here, CRS, multifocusing and i-CRS display the same behavior for other values of R .

Migrated amplitudes

Kirchhoff-type time migration aims to collapse diffractions in the stack to their respective apex locations in midpoint and time. The resulting amplitudes are therefore a measure for the quality of the attributes and the stack. We have applied an attribute-based poststack time migration (Mann, 2002) to the stacks and parameters obtained from the datasets with $R=10$ m.

[Figure 8 about here.]

The results are shown in Figure 8 for gradients from $\gamma=0$ to 1.5/s. We observe that CRS leads to lower amplitudes and lower resolution than i-CRS and multifocusing, but it maintains the amplitude for all gradients. Classical multifocusing leads to a focused diffractor, however, the amplitude degrades strongly with increasing gradient. i-CRS also leads to a focused image. Although its amplitude also decreases with higher gradient strength, the effect is far less pronounced than for multifocusing. Again, we conclude that the i-CRS op-

erator combines the stability of CRS regarding heterogeneities with the better performance of multifocusing in the presence of diffractions.

COMPLEX SYNTHETIC EXAMPLE

Our tests so far have indicated the i-CRS operator performs better in the presence of vertical heterogeneities. For time processing with symmetric analytic operators the vertically inhomogeneous model appears to be the most appropriate choice for a quantitative test. In field data processing, however, we are also faced with lateral heterogeneities. Therefore we apply the CRS, conventional multifocusing and i-CRS method to a complex synthetic example in this section.

[Figure 9 about here.]

The Sigsbee 2a dataset is widely used to test the potential of new time imaging methods. This is due to the fact that almost all challenging features are present in the underlying geological setting, which is illustrated in Figure 9. The top-of-salt is structurally very complex and of rugged character, resulting in numerous diffractions in the data. In addition, steep flanks and connected synclinal structures cause triplications. The two horizontal lines of equally spaced point diffractors in the sediment beddings reach beneath the salt. Due to the large lateral and vertical extent of the salt body, especially deeper parts of the model are only sparsely illuminated.

Semblance and stack

Figure 10 shows the semblance difference between CRS and i-CRS (Figure 10(a)) and between conventional multifocusing and i-CRS (Figure 10(b)). We observe that CRS, mul-

tifocusing and the implicit CRS approximate the response from the mostly unperturbed smoothly curved strata above the top-of-salt with similar quality. Moreover, events connected with discontinuities left of the salt body are equivalently described by all three operators.

[Figure 10 about here.]

The main deviations in semblance between conventional CRS and i-CRS can be attributed to the steep flanks of the diffraction patterns, stemming either from the highly-curved features of the rugged top-of-salt or from the two horizons of equally spaced point diffractors. While CRS only provides a sufficient description in a very small vicinity of the diffraction’s apex, application of the implicit CRS approach leads to high semblance values even for very large horizontal displacements (compare Figure 5). In particular, diffractions from the top-of-salt are poorly described by the hyperbolic CRS operator, whereas i-CRS provides a superior fit. For events that stem from diffracting structures located in the deeper parts of the model, i-CRS also displays a noticeably improved fit.

Since the macro-velocity gradient is moderate in the upper part of the model, conventional multifocusing and implicit CRS perform equally well for the very prominent events connected to the top-of salt, as can be seen in Figure 10(b)). However, in deeper parts of the section, e.g. at 4000 m lateral position and 9.5 s TWT, application of i-CRS leads to noticeably higher semblance values for highly-curved features.

It is important to note the scale at this point. For almost all diffraction events, application of the new operator leads to an increase in semblance of at least 0.2 up to 0.6, compared to CRS, meaning that large portions of most diffraction events in the data are described twice as well.

The findings for the semblance section also apply to the actual stacks. Figure 11 shows the stacked section for i-CRS and a closeup for all three methods. The quality of the stacked sections is equally good for nearly planar reflectors in the model. For diffraction events, application of i-CRS and classical multifocusing leads to noticeably higher amplitudes and better resolution than CRS. In addition, the stacked waveforms in the i-CRS section also show less distortions than the respective counterparts in the CRS-stacked section. In conclusion, the significantly better fit of the implicit operator to diffraction events in the prestack data not only leads to higher values of semblance, but also to an improved simulated zero-offset section.

[Figure 11 about here.]

Attributes

Unlike in the generic example above, we cannot compare the obtained attributes to reference values for our complex example. Therefore, we use the results of the attribute-based poststack time migration (Mann, 2002) to evaluate the quality of the attributes. Figure 12 shows the time-migrated image using the i-CRS result and closeups of the results for all three methods.

[Figure 12 about here.]

The attribute estimates of both double-square-root type operators, i-CRS and multifocusing, allow for a significant focusing of diffracted energy. In contrast, we observe that diffraction events in the CRS-stacked section are overall not optimally collapsed for the top-of-salt, whereas i-CRS and classical multifocusing lead to comparable results. In the

deeper parts we find the same behavior for CRS, and a slightly better focusing in the i-CRS section (see Figure).

Again, we find confirmed that i-CRS combines the strengths of conventional CRS and multifocusing, leading to a good performance over the full reflector curvature range. This holds even in deeper parts of the model, where the velocity variations in the overburden have higher impact. Note that for all considered examples, the application of a single iteration step in the angle update, i.e., $n=1$ in equation 11, already led to sufficient accuracy.

CONCLUSIONS

We have introduced a new implicit CRS approach that combines the double-square-root character of the multifocusing approach and the parameterization of the conventional CRS formula. The new approximation considers a locally circular interface and leads to a double-square-root type operator that is expressed in terms of CRS parameters. Its implicit character favors an efficient iterative implementation; however, already a single iteration leads to high accuracy. For common acquisition and subsurface configurations, the new approach reduces to familiar formulae.

A quantitative study with generic examples revealed that the new approach leads to high accuracy in traveltime and attributes for reflector curvatures, ranging from the diffraction limit to nearly planar reflectors, as well as heterogeneities. It thus combines the advantage of the CRS operator, robustness regarding velocity variations, with the advantage of conventional multifocusing as a double-square-root type expression. Consequently, in our systematic investigation of generic examples, the new approach delivered consistently reliable attribute estimates even for strong gradients, whereas CRS and multifocusing where

either affected by reflector curvature or inhomogeneity.

The results of the quantitative studies confirm these conclusions for a more complex subsurface setting. Applied to the Sigsbee 2a synthetic dataset, the new approach performs well for all curvatures and even in deep parts of the model, where lateral velocity changes in the overburden become more pronounced. Compared to conventional CRS, i-CRS provides a significantly better focused stack, in particular for steep events and diffractions. Furthermore, the wavefield attributes determined with the i-CRS method are of superior quality compared to those obtained from CRS, resulting in a further increase in resolution in the time-migrated section.

OUTLOOK

Future work includes the application of i-CRS to field data. The formulation of the method in three dimensions and for common-offset is investigated. Another future aspect is the performance of i-CRS for the separation of diffraction and reflection events (Dell and Gajewski, 2011). A modified i-CRS description capable to account for anisotropy and converted waves has recently been developed by Vanelle et al. (2012).

ACKNOWLEDGMENTS

We thank the members of the Applied Seismics Group Hamburg for continuous discussions. The suggestions and remarks by the anonymous reviewers helped to improve the quality of this paper and are very appreciated. Special thanks go to Jürgen Mann for providing the CRS code. Seismic Un*x routines were used for the generation of the generic examples. The Sigsbee 2a synthetic data were produced by the Subsalt Multiples Attenuation and

Reduction Technology Joint Venture (SMAART JV). This work was partly supported by the sponsors of the Wave Inversion Technology (WIT) Consortium and the project 'Imaging steep structures with diffractions', which is funded by the German Ministry of Environment (BMU 0325363C).

REFERENCES

- Baykulov, M., S. Dümmong, and D. Gajewski, 2011, From time to depth with CRS attributes: *Geophysics*, **76**, S151–S155.
- de Bazelaire, E., 1988, Normal moveout revisited – inhomogeneous media and curved interfaces: *Geophysics*, **53**, 143–157.
- Dell, S., and D. Gajewski, 2011, Common-reflection-surface-based workflow for diffraction imaging: *Geophysics*, **76**, 187–195.
- Drexler, M., and M. J. Gander, 1998, Circular billiard: *SIAM Review*, **40**, 315–323.
- Dümmong, S., and D. Gajewski, 2008, A multiple suppression method via CRS attributes: SEG Technical Program Expanded Abstracts 2008, doi: 10.1190/1.3063869.
- Duveneck, E., 2004, Velocity model estimation with data-driven wavefront attributes: *Geophysics*, **69**, 265–274.
- Fomel, S., and V. Grechka, 2001, Nonhyperbolic reflection moveout of P-waves: An overview and comparison of reasons: Technical report CWP-372, Colorado School of Mines. (<http://www.cwp.mines.edu/Meetings/Project01/cwp372.pdf>).
- Fomel, S., and R. Kazinnik, 2012, Non-hyperbolic common reflection surface: *Geophysical Prospecting*, 1–7, doi: 10.1111/j.1365–2478.2012.01055.x.
- Gelchinsky, B., A. Berkovitch, and S. Keydar, 1999, Multifocusing homeomorphic imaging – part 1. Basic concepts and formulae: *Journal of Applied Geophysics*, **42**, 229–242.
- Hertweck, T., J. Schleicher, and J. Mann, 2007, Data stacking beyond CMP: The Leading Edge, **26**, 818 – 827.
- Höcht, G., E. de Bazelaire, P. Majer, and P. Hubral, 1999, Seismics and optics: hyperbolae and curvatures: *Journal of Applied Geophysics*, **42**, 261–281.
- Hubral, P., 1983, Computing true amplitude reflections in a laterally inhomogeneous earth:

- Geophysics, **48**, 1051–1062.
- Jäger, R., J. Mann, G. Höcht, and P. Hubral, 2001, Common-reflection-surface stack: Image and attributes: Geophysics, **66**, 97–109.
- Keydar, S., B. Gelchinsky, V. Shtivelman, and A. Berkovitch, 1990, Common evolute element (CEE) stack and imaging (zero-offset stack): SEG Technical Program Expanded Abstracts 1990, doi: 10.1190/1.1890107.
- Khaidukov, V., E. Landa, and T. J. Moser, 2004, Diffraction imaging by focusing-defocusing: An outlook on seismic superresolution: Geophysics, **69**, 1478–1490.
- Landa, E., 2007, Beyond conventional seismic imaging: EAGE.
- Landa, E., S. Keydar, and T. J. Moser, 2010, Multifocusing revisited – inhomogeneous media and curved interfaces: Geophysical Prospecting, **58**, 925–938.
- Mann, J., 2002, Extensions and Applications of the Common-Reflection-Surface Stack Method: PhD thesis, Universität Karlsruhe.
- Mayne, W. H., 1962, Common reflection point horizontal data stacking techniques: Geophysics, **27**, 927–938.
- Neumann, P. M., 1998, Reflections on reflection in a spherical mirror: American Mathematical Monthly, **105**, 523–528.
- Schleicher, J., M. Tygel, and P. Hubral, 1993, Parabolic and hyperbolic paraxial two-point traveltimes in 3D media: Geophysical Prospecting, **41**, 495–514.
- Schwarz, B., C. Vanelle, B. Kashtan, and D. Gajewski, 2012, i-CRS – application of a new multi-parameter stacking approach to complex media: SEG Technical Program Expanded Abstracts 2012, doi: 10.1190/segam2012–1542.1.
- Tygel, M., T. Müller, P. Hubral, and J. Schleicher, 1997, Eigenwave based multiparameter traveltime expansions: SEG Technical Program Expanded Abstracts 1997, doi:

10.1190/1.1885776.

Vanelle, C., M. Bobsin, P. Schemmert, B. Kashtan, and D. Gajewski, 2012, i-CRS – a new multiparameter stacking operator for an/isotropic media: SEG Technical Program Expanded Abstracts 2012, doi: 10.1190/segam2012-0588.1.

LIST OF FIGURES

1	Illustration of the meaning of the three CRS attributes α , R_{NIP} and R_N . .	29
2	Acquisition and subsurface geometry for the circular reflector (a). For zero-offset, the angle θ is an explicit expression (b). For non-vanishing offsets it is obtained recursively and the zero-offset angle θ_0 serves as a starting guess (c). The quantities $x_s = x_m - h$ and $x_g = x_m + h$ denote the source and receiver locations, respectively. For increasing number of iterations n , the updated angle θ_n approaches the actual reflection point angle θ	30
3	The underlying model of the quantitative study. Grayscale is proportional to velocity.	31
4	RMS errors of i-CRS for $R = 10,000$ m, varying number of iterations, and different gradient strengths. While for the constant velocity case ($\gamma = 0$) an increase of the number of iterations leads to high accuracy up to machine precision, the iteration does not lead to smaller RMS errors for non-zero gradients. Please note the logarithmic scale.	32
5	Semblance distribution over gradient strength and displacement from the apex for (a) conventional CRS, (b) conventional multifocusing and (c) i-CRS. Shown are the extreme cases of $R = 10$ m and $R = 10000$ m. For low reflector curvature, all considered operators perform equally well, whereas for high curvatures the approximations behave very differently.	33
6	RMS error distributions for (a) i-CRS and CRS and (b) i-CRS and conventional multifocusing.	34
7	Comparison of the extracted parameters to exact values for (a) the emergence angle α , (b) the radius of the NIP -wave, and (c) the curvature of the normal wave for $R=10$ m (i.e., the diffraction limit) and $\gamma=0.5/s$	35
8	Absolute stacked amplitude resulting from the attribute-based poststack time migration for $R = 10$ m and all considered gradients.	36
9	The underlying model of the Sigsbee 2a synthetic dataset simulates a realistic and complex geological setting.	37
10	Semblance difference between (a) conventional CRS and i-CRS and (b) conventional multifocusing and i-CRS. Please note the different scales.	38
11	Stacked section (a) and closeup comparison (b) for the complex Sigsbee 2a synthetic dataset.	39
12	Time-migrated image (a), comparison for the top-of-salt and a subsalt point diffractor (b) of the Sigsbee 2a model.	40

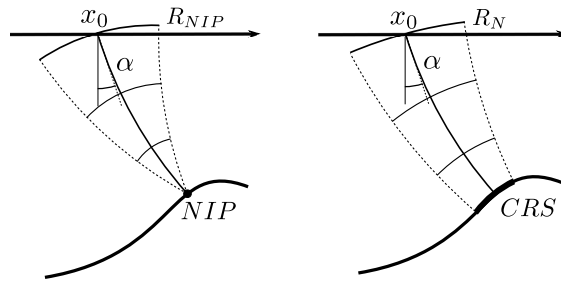


Figure 1: Illustration of the meaning of the three CRS attributes α , R_{NIP} and R_N .

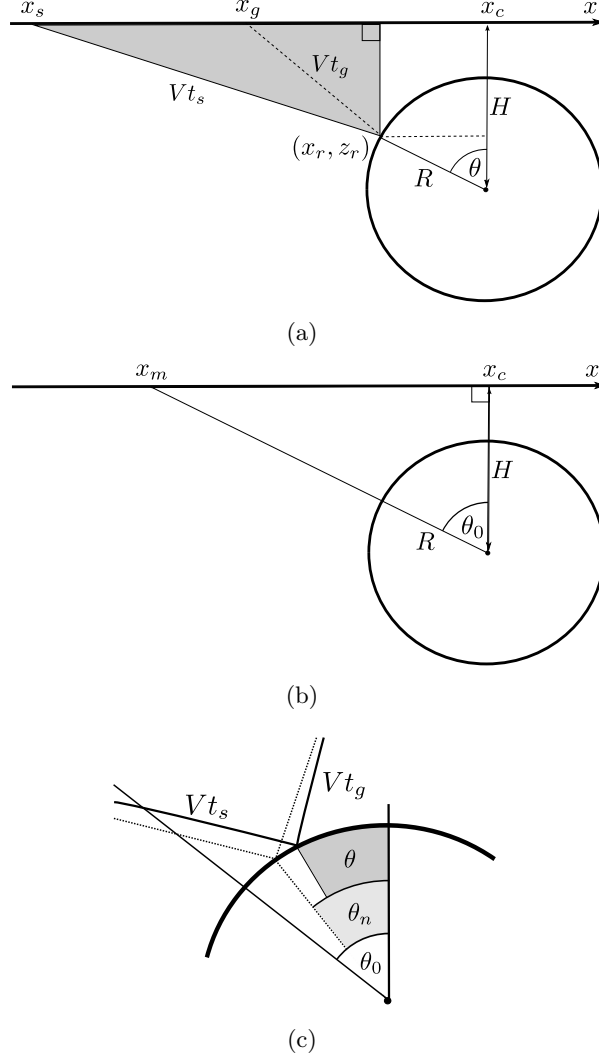


Figure 2: Acquisition and subsurface geometry for the circular reflector (a). For zero-offset, the angle θ is an explicit expression (b). For non-vanishing offsets it is obtained recursively and the zero-offset angle θ_0 serves as a starting guess (c). The quantities $x_s = x_m - h$ and $x_g = x_m + h$ denote the source and receiver locations, respectively. For increasing number of iterations n , the updated angle θ_n approaches the actual reflection point angle θ .

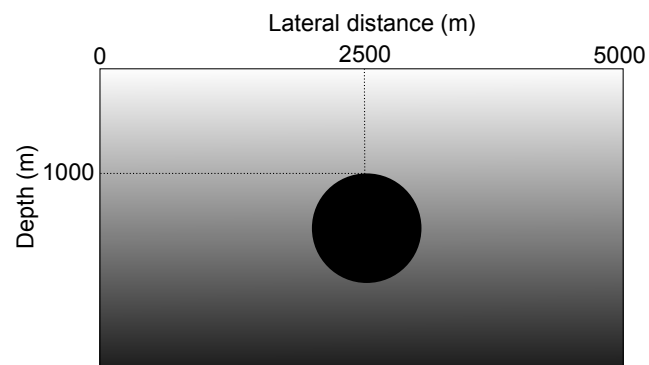


Figure 3: The underlying model of the quantitative study. Grayscale is proportional to velocity.

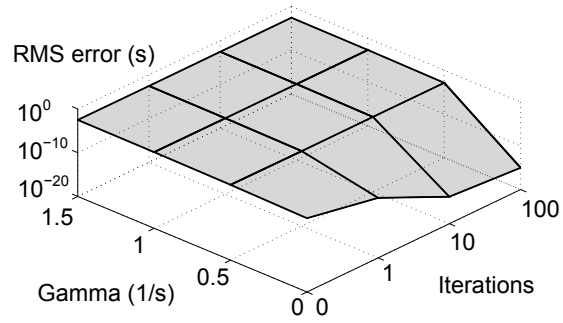


Figure 4: RMS errors of i-CRS for $R = 10,000$ m, varying number of iterations, and different gradient strengths. While for the constant velocity case ($\gamma = 0$) an increase of the number of iterations leads to high accuracy up to machine precision, the iteration does not lead to smaller RMS errors for non-zero gradients. Please note the logarithmic scale.

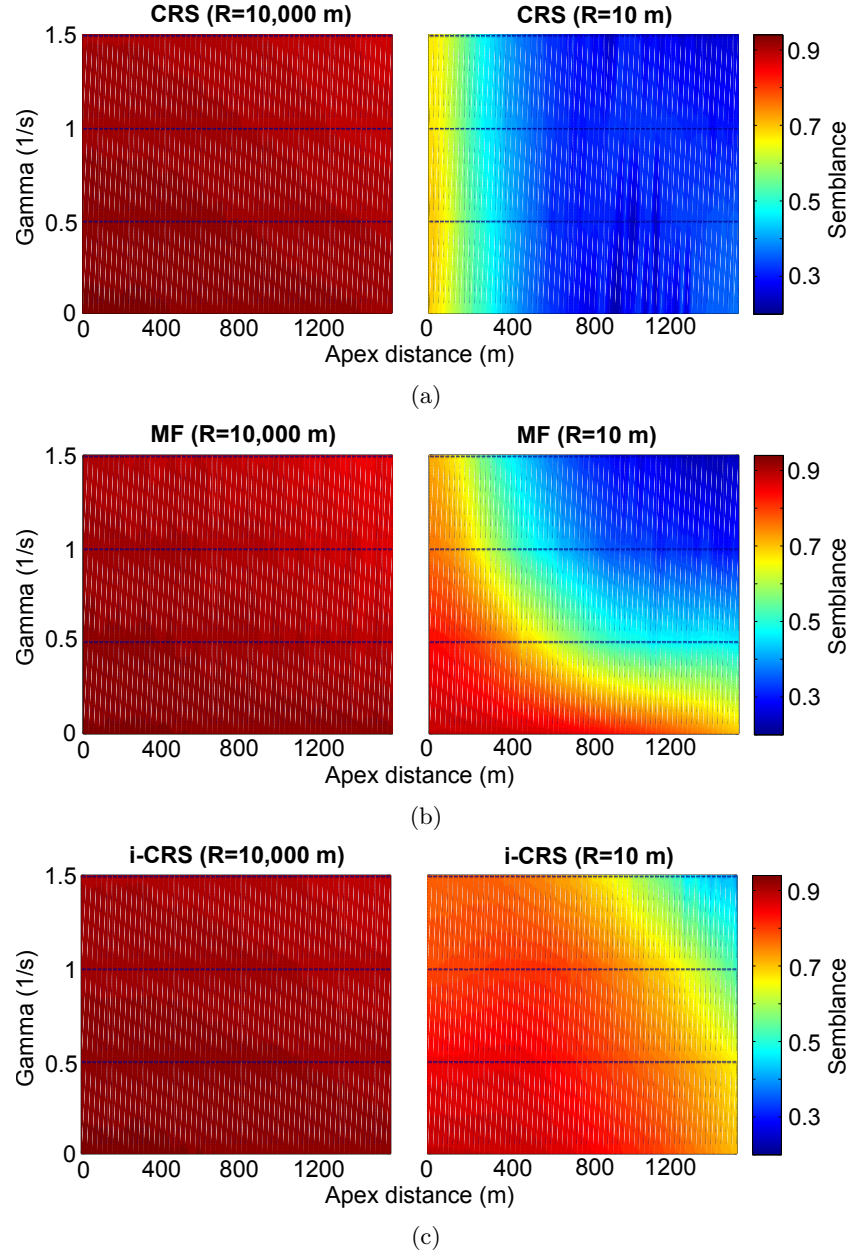
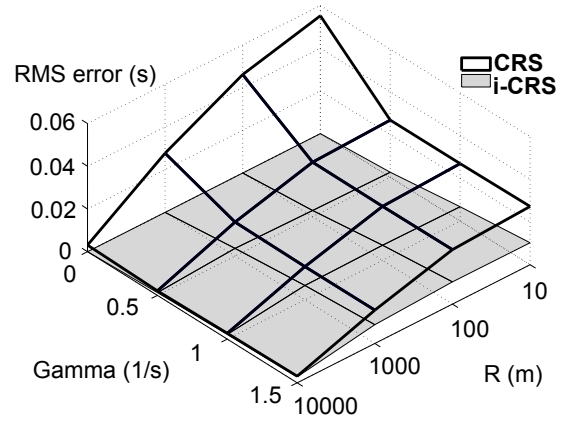
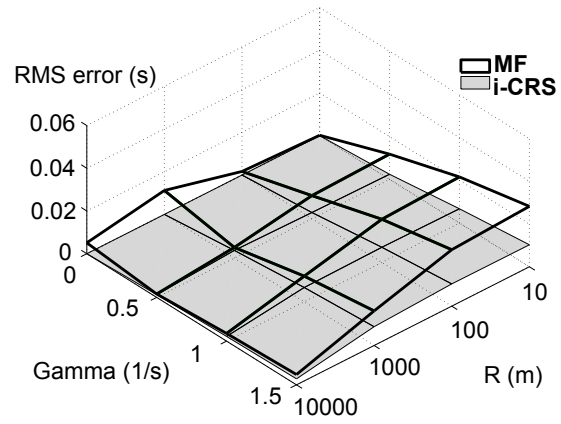


Figure 5: Semblance distribution over gradient strength and displacement from the apex for (a) conventional CRS, (b) conventional multifocusing and (c) i-CRS. Shown are the extreme cases of $R = 10$ m and $R = 10000$ m. For low reflector curvature, all considered operators perform equally well, whereas for high curvatures the approximations behave very differently.

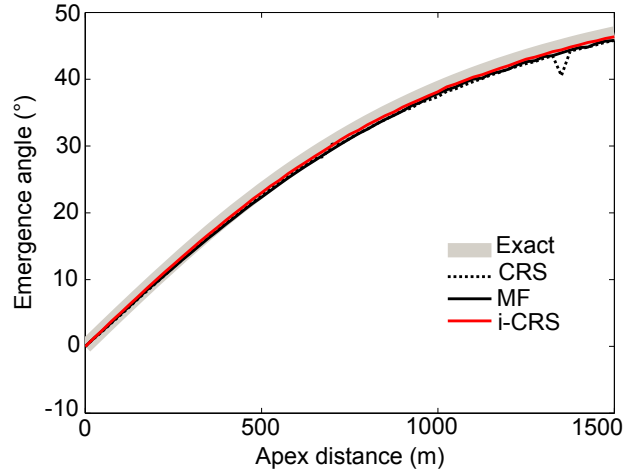


(a)

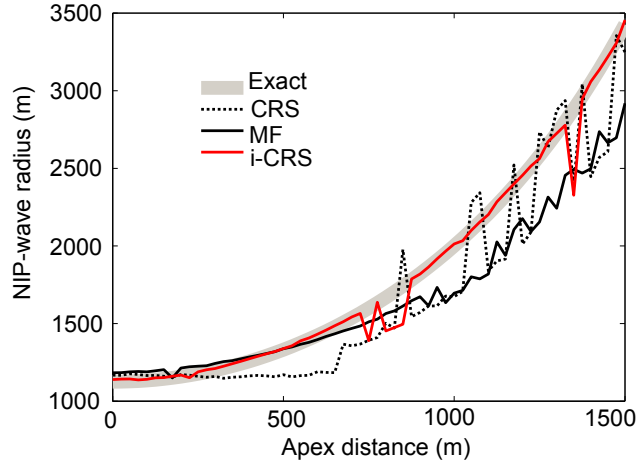


(b)

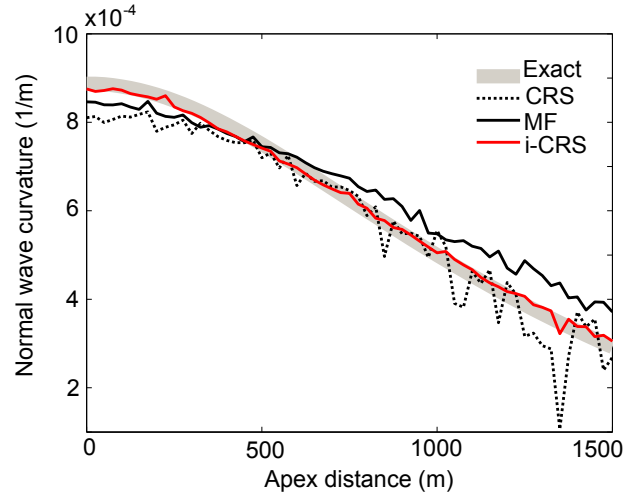
Figure 6: RMS error distributions for (a) i-CRS and CRS and (b) i-CRS and conventional multifocusing.



(a)



(b)



(c)

Figure 7: Comparison of the extracted parameters to exact values for (a) the emergence angle α , (b) the radius of the *NIP*-wave, and (c) the curvature of the normal wave for $R=10$ m (i.e., the diffraction limit) and $\gamma=0.5/s$.

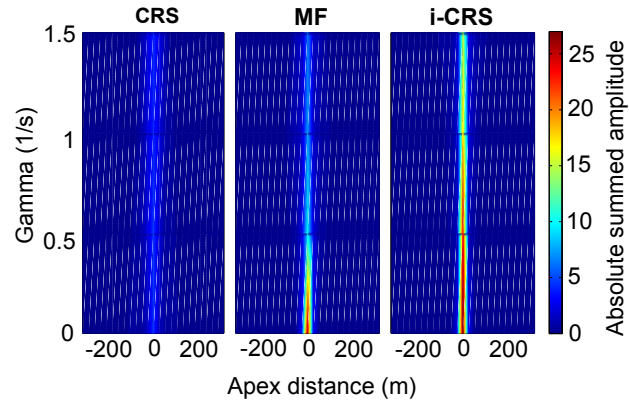


Figure 8: Absolute stacked amplitude resulting from the attribute-based poststack time migration for $R = 10$ m and all considered gradients.

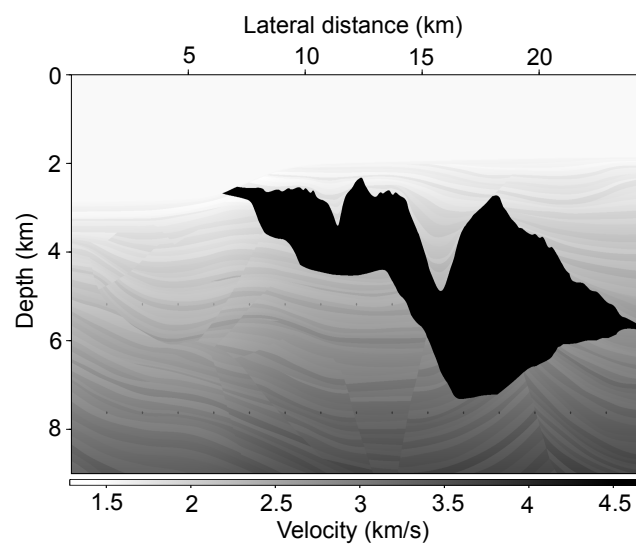


Figure 9: The underlying model of the Sigsbee 2a synthetic dataset simulates a realistic and complex geological setting.

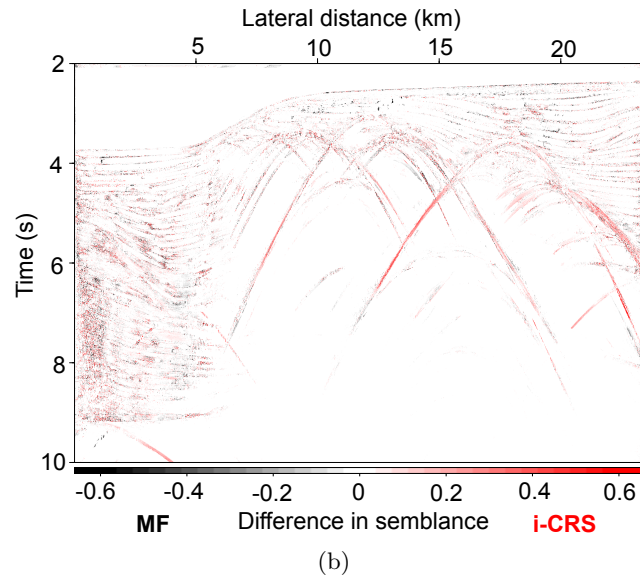
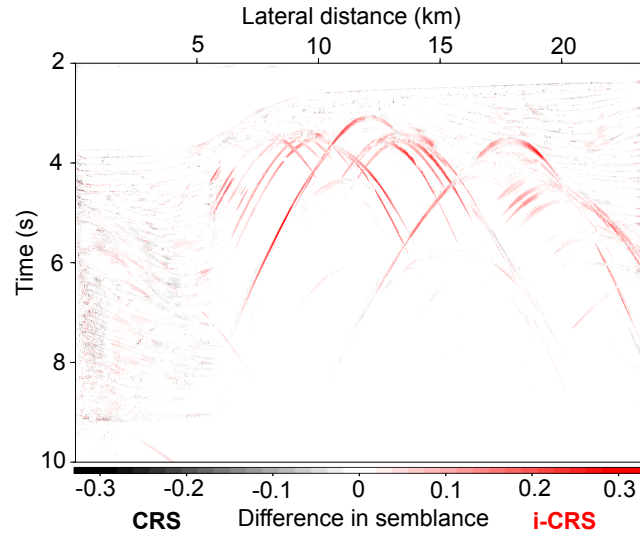


Figure 10: Semblance difference between (a) conventional CRS and i-CRS and (b) conventional multifocusing and i-CRS. Please note the different scales.

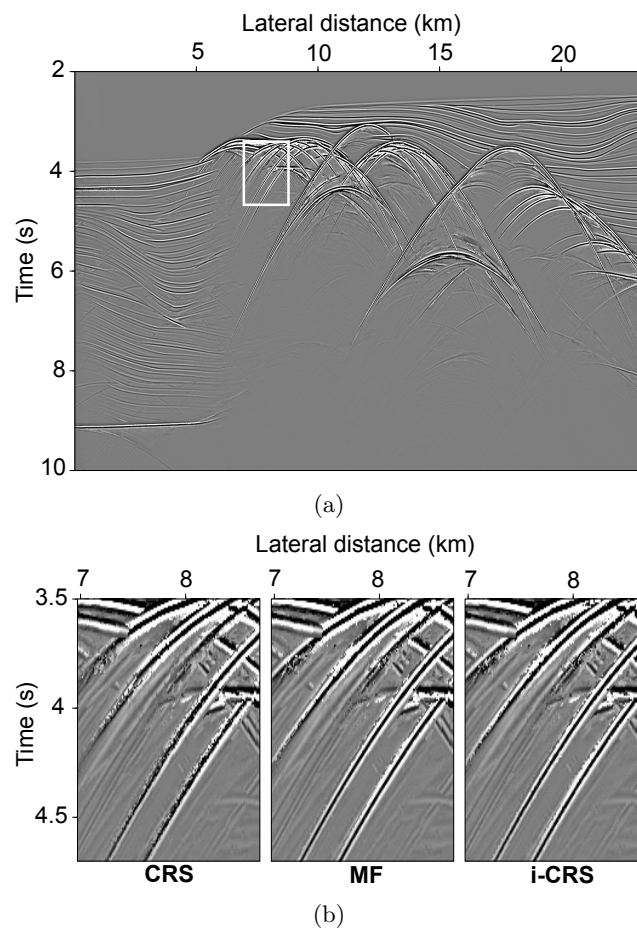
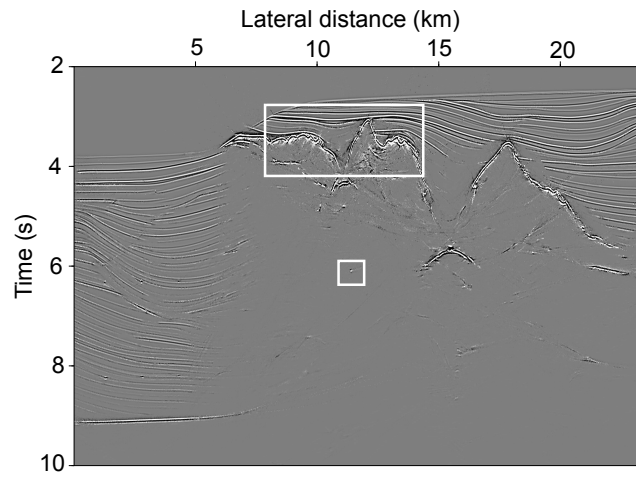
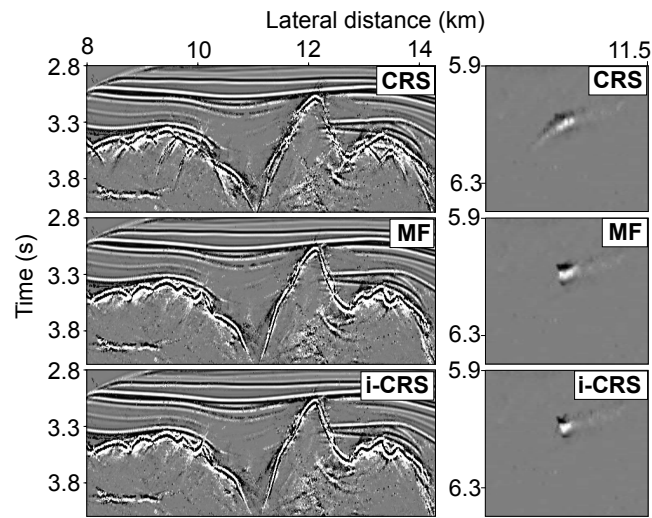


Figure 11: Stacked section (a) and closeup comparison (b) for the complex Sigsbee 2a synthetic dataset.



(a)



(b)

Figure 12: Time-migrated image (a), comparison for the top-of-salt and a subsalt point diffractor (b) of the Sigsbee 2a model.